

Computationally Driven Discovery of Quaternary Tantalum-Based MAB-Phases: $\text{Ta}_4\text{M}''\text{SiB}_2$ ($\text{M}'' = \text{V}, \text{Cr}, \text{or Mo}$): Synthesis, Characterization, and Elastic Properties

Ahmed S. Etman,^{*,§} Joseph Halim,[§] Hans Lind, Megan Dorri, Justinas Palisaitis, Jun Lu, Lars Hultman, Per O. Å. Persson, and Johanna Rosen^{*}



Cite This: *Cryst. Growth Des.* 2023, 23, 4442–4447



Read Online

ACCESS |



Metrics & More

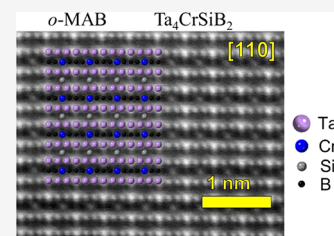


Article Recommendations



Supporting Information

ABSTRACT: We report on the synthesis of computationally predicted out-of-plane chemically ordered transition metal borides labeled *o*-MAB phases, $\text{Ta}_4\text{M}''\text{SiB}_2$ ($\text{M}'' = \text{V}, \text{Cr}$), and a structurally equivalent disordered solid solution MAB phase $\text{Ta}_4\text{MoSiB}_2$. The boride phases were prepared using solid-state reaction sintering of the constituting elements. High-resolution scanning transmission electron microscopy along with Rietveld refinement of the powder-X-ray diffraction patterns revealed that the synthesized *o*-MAB phases $\text{Ta}_4\text{CrSiB}_2$ (98 wt % purity) and Ta_4VSiB_2 (81 wt % purity) possess chemical ordering with Ta preferentially residing in the 16l position and Cr and V in the 4c position, whereas $\text{Ta}_4\text{MoSiB}_2$ (46 wt % purity) was concluded to form a disordered solid solution. Density functional theory (DFT) calculations were used to investigate the dynamic stability, elastic properties, and electronic density states for the MAB phases, confirming the stability and suggesting the borides based on Cr and Mo to be stiffer than those based on V and Nb.



INTRODUCTION

Transition metal carbides and borides are two families of ceramic materials with very useful properties such as good thermal stability owing to their high melting point^{1,2} and excellent mechanical properties due to their high hardness and low compressibility.^{1,2} In the last decade, tremendous research efforts have been done on exploring these ceramic materials. The most well-known class of layered ceramics is the family of transition metal nitrides or carbides, so-called MAX phases. The MAX phases have a general formula $(\text{M}_{n+1}\text{AX}_n)$,^{3,4} where $n = 1, 2, 3$, or 4, M = transition metal (e.g., Ti, V, Mo, Nb or Cr), A = an element from group IIIA or IVA (e.g., Al or Si), and X = C or N. Selective etching of specific layers of MAX phases results in a class of 2D materials known as MXene⁵ showing promise for a wide range of applications, including outstanding electrochemical and catalytic properties.⁶

A family of materials resembling the MAX phases are layered ceramics based on B, called MAB phases. The MAB phases are chemically diverse and can exist in a variety of crystal structures, involving orthorhombic $\text{M}_{n+1}\text{AB}_{2n}$ ($n = 1-3$),¹ hexagonal M_2AB_2 ,⁷ monoclinic $\text{M}_{n+1}\text{AB}_n$ ($n = 1, 2$),^{8,9} and the tetragonal M_3AB_2 (also known as T2 phases).¹⁰ So far, a variety of T2 phases have been prepared, including Mo_5SiB_2 ,¹⁰ W_5SiB_2 ,¹⁰ Fe_5SiB_2 ,¹¹ and Mn_5SiB_2 ,¹¹ possessing unique chemical (e.g., high oxidation stability¹²) and physical (good elasticity² and superconductivity¹³) properties.

To expand the chemistry of the MAB phase family and include more transition metals, many attempts have been made to synthesize quaternary MAB phases based on two M elements, forming either a disordered solid solution or

chemical order. As an example of the latter, a MAB phase with in-plane ordering, $(\text{Mo}_{2/3}\text{Sc}_{1/3})_2\text{AlB}_2$, was recently reported, obtained from solid-state reaction sintering in which the molar ratio of Mo and Sc was about 2:1.¹⁴ Notably, this so called *i*-MAB phase could be selectively etched into a 2D material, $\text{Mo}_{4/3}\text{B}_2$, being referred to as boridene or MBene,¹⁵ showing good catalytic properties.¹⁶

Similarly, by adding Mo to Ti_5SiB_2 (a T2 phase) in a ratio of Ti/Mo equal to 4:1, out-of-plane chemical order could be established, thereby forming a so called *o*-MAB phase, $\text{Mo}_4\text{TiSiB}_2$.¹⁷ This phase could be converted into single sheets of 2D TiO_xCl_y .¹⁷ Later on, Dahlqvist and Rosen reported a systematic theoretical protocol to predict the stability of quaternary MAB phases derived from T2 phases with a general formula $\text{M}_4'\text{M}''\text{AB}_2$, where A = Al, Si, P, Ga, Ge, In, and Sn.¹⁸ These quaternary MAB phases can either be *o*-MAB phases with out-of-plane chemical order or disordered solid solutions.¹⁸ Notably, the study predicted 35 *o*-MAB phases as well as 121 solid solutions, showing that alloying is a fruitful pathway for expanding the concept of T2 phases to include novel elemental combinations. To date, $\text{Mo}_4\text{TiSiB}_2$ is the only member of the *o*-MAB phases to be experimentally reported;¹⁷

Received: February 22, 2023

Revised: May 11, 2023

Published: May 23, 2023



accordingly, there is a need to develop experimental approaches to also realize other members of this *o*-MAB phase family.

Inspired by the properties of quaternary MAB phases and the recently synthesized MBene,¹⁵ herein, we report computationally driven synthesis and characterization of quaternary tantalum-based *o*-MAB phases, in particular, Ta₄CrSiB₂ and Ta₄VSiB₂. Also, Ta₄MoSiB₂ was investigated, showing preference for chemical disordered solutions (a solid solution). The structure, composition (sample purity), and chemical ordering of the prepared phases were investigated using X-ray diffraction (XRD), scanning electron microscopy (SEM) equipped with an energy dispersive X-ray (EDX) detector, and atomically resolved high-resolution scanning transmission electron microscopy (HR-STEM) analyses. Furthermore, using density functional theory (DFT) calculations, we predicted the dynamic stability, elastic properties, and electronic density states of the materials investigated herein.

RESULTS AND DISCUSSION

The characteristic crystal structure of Ta₄M''SiB₂ phases for out-of-plane chemical ordering is presented in Figure 1 along

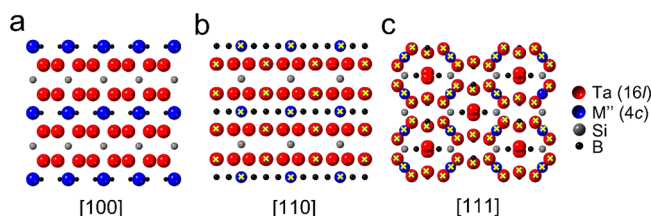


Figure 1. Crystal structure of chemically out-of-plane ordered *o*-MAB phases, Ta₄M''SiB₂, shown for three zone axes: (a) [100], (b) [110], and (c) [111]. The projected atoms with yellow crosses in images b and c, as well as all metal atoms in image a (i.e., all red and blue spheres in image a), have an equivalent number of atoms in their corresponding atomic columns along the shown zone axes. Hence, they can be used to conclude chemical ordering based on contrast in HR-STEM images due to the atomic mass difference between Ta and M''.

the primary [100], [110], and [111] zone axes. The chemical ordering can be revealed using atomically resolved HR-STEM imaging by observing the contrast differences between the transition metal atomic columns along [100] (see Figure 1a) as well as the transition metal atomic columns marked by yellow crosses along the [110] and [111] zone axes (see Figure 1b,c). Since the atomic columns along these axes have the same number atoms in the projection, the observed contrast differences can be attributed to the mass contrast between Ta and M''.

The Ta₄M''SiB₂ phases were prepared using solid-state reaction sintering of the constituting elements as described in the experimental section. The morphology and composition of the prepared boride phases were examined by SEM imaging and EDX analysis (see Figure S1). The EDX data quantification showed that the atomic ratios of Ta/Cr/Si in Ta₄CrSiB₂ were 66:16:18 at % (see Table S2) which agrees well with the theoretical atomic ratios of the elements of about 4:1:1.

The atomic structure and sample purity of the boride phases were analyzed using a combination of HR-STEM imaging as well as XRD with Rietveld refinement. HR-STEM images for Ta₄CrSiB₂ matched the simulated structure model along the

[110] and [100] zone axes quite well (see Figure 2a,b). Furthermore, the observed mass contrast in the HR-STEM images confirmed the chemical ordering of Ta and Cr (see Figure 2a,b). It should be noted that Ta is heavier than Cr; therefore, the brighter atomic columns in HR-STEM images should represent Ta and darker atomic columns represent the Cr atoms. The T2 phases have a tetragonal crystal structure of *I4/mcm* symmetry, where the Ta and Cr elements occupy the two different Wyckoff sites 16l and 4c, respectively. In addition, the Si and B atoms are not resolved under the applied HR-STEM imaging conditions due to being relatively light elements compared to Ta and Cr.

XRD analysis combined with Rietveld refinement showed that the experimentally observed pattern (black crosses in Figure 2c) matches the simulated (calculated) pattern based on the structure model (red line in Figure 2c). The differences between the experimental and the calculated pattern are small, as shown by the blue line in Figure 2c. The Rietveld refinement showed a high purity of the prepared Ta₄CrSiB₂ sample (98.7 wt %) with χ^2 about 7.96. The amount of the impurity phase, TaB, was approximately 1.3 wt % (see Table S3). The structure analysis of Ta₄CrSiB₂ showed a typical T2 structure with a tetragonal unit cell ($a = b = 6.072(6)$ Å; $c = 11.465(1)$ Å) and *I4/mcm* symmetry. The detailed refinement data are summarized in Tables S3 and S4.

Ta₄VSiB₂ was similarly prepared using solid-state reaction sintering as discussed in the experimental section. The SEM combined with EDX analysis showed that the atomic ratios of Ta/V/Si in the experimentally prepared Ta₄VSiB₂ were 65:17:18 at % (see Figure S1 and Table S2) which is in good agreement with the theoretical values (4:1:1). HR-STEM imaging revealed a chemically ordered structure of Ta₄VSiB₂ phase, as shown by a HR-STEM image along the [100] zone axis (see Figure 3a). From a difference in contrast, it can be concluded that the Ta and V elements primarily occupy the two different Wyckoff sites 16l and 4c, respectively. The XRD pattern of the experimentally prepared Ta₄VSiB₂ (black crosses in Figures 3b and S2) matched well the simulated XRD pattern (red line in Figures 3b and S2). Rietveld refinement for the XRD pattern (with χ^2 about 6.33) displayed a sample purity of Ta₄VSiB₂ of about 81.0 wt % and the presence of the impurity phases TaB, Ta₅SiB₂, Ta₂B, and V₃Si, with an estimated content as shown in Table S3. Rietveld refinement also showed that Ta₄VSiB₂ has a typical T2 structure with a tetragonal unit cell ($a = b = 6.123(4)$ Å; $c = 11.456(1)$ Å; $\alpha = \beta = \gamma = 90.0^\circ$) and *I4/mcm* symmetry (see Table S4).

The Ta₄MoSiB₂ showed the lowest purity among the three prepared boride samples, 41 wt %, with the ternary Ta₅SiB being the majority phase of the sample, of 46.2 wt %, as seen from the Rietveld refinement (see Tables S3 and S4). Other competing phases were TaB, Mo₂B, and MoB₂ although they are of minor concentrations. Based on DFT calculations and thermodynamic considerations, including effects from entropy (see Note S1 and ref 17), the Ta₄MoSiB₂ phase prefers the formation of a disordered solid solution of Ta and Mo. HR-STEM imaging along the [100] and [111] zone axes confirmed a disordered metal arrangement in Ta₄MoSiB₂ (see Figure S3) since no relative contrast differences could be distinguished (cf. Ta₄CrSiB₂ and Ta₄VSiB₂ above). Still, Rietveld refinement indicated that Ta₄MoSiB₂ has a T2 structure with a tetragonal unit cell ($a = b = 6.166(3)$ Å; $c = 11.485(9)$ Å; $\alpha = \beta = \gamma = 90.0^\circ$) and *I4/mcm* symmetry (see Figure 3c and Table S4).

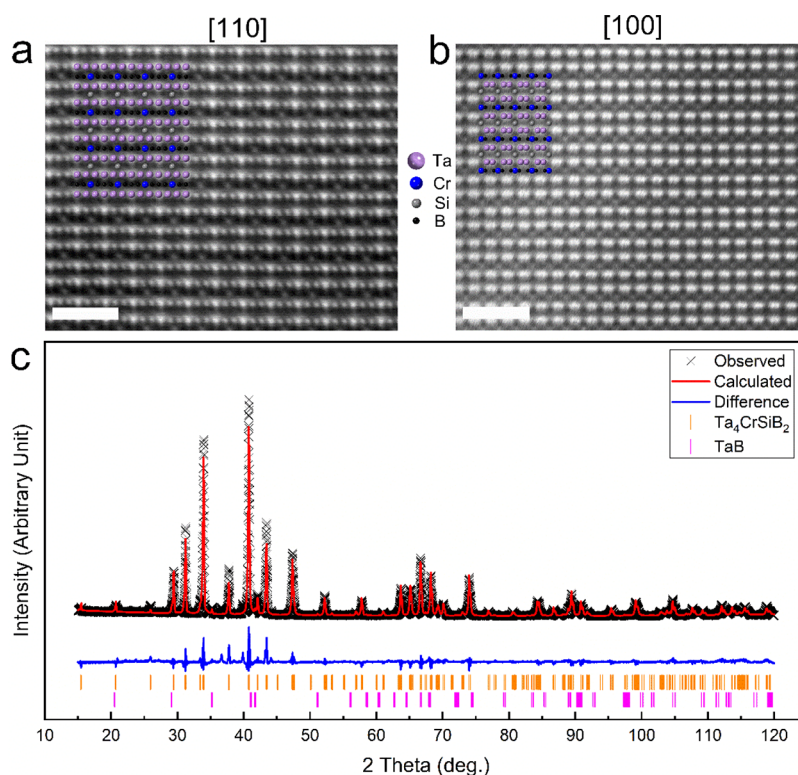


Figure 2. Structure of the $\text{Ta}_4\text{CrSiB}_2$ *o*-MAB phase: (a) and (b) HR-STEM images of $\text{Ta}_4\text{CrSiB}_2$ along the zone axes $[110]$ and $[100]$, respectively. The schematic crystal structure for each zone axis is overlaid on its respective HR-STEM image. The scale bar in (a) and (b) is 1 nm. (c) XRD pattern of the $\text{Ta}_4\text{CrSiB}_2$ sample showing the measured pattern (black crosses), Rietveld generated simulated pattern (red line), and the difference between both patterns (blue line). The orange and pink ticks represent the peak positions of the phases $\text{Ta}_4\text{CrSiB}_2$ and TaB, respectively.

DFT calculations were performed for the $\text{Ta}_4\text{M}''\text{SiB}_2$ phases with $\text{M}'' = \text{V}, \text{Cr}, \text{Nb}$, and Mo . The $\text{Ta}_4\text{NbSiB}_2$ phase was included in the theoretical analysis to allow a comparison between boride phases with M'' elements from group V (i.e., V and Nb) and group VI (i.e., Cr and Mo) in the periodic table of elements, all of which have been reported thermodynamically stable (from theory) as a solid solution (M'' equal to Nb and Mo) or in the form of an *o*-MAB phase (M'' equal to Cr and V).¹⁸ A theoretical analysis including the relative stability between ordered and disordered boride phases is summarized in the supporting information Note S1 and Table S5, in line with previous work.¹⁸ The theoretical results presented are therefore for disordered solid solutions $\text{Ta}_4\text{MoSiB}_2$ and $\text{Ta}_4\text{NbSiB}_2$ and for chemically ordered *o*-MAB phases $\text{Ta}_4\text{CrSiB}_2$ and Ta_4VSiB_2 , unless otherwise noted.

The magnetic configuration of the Cr atoms was tested as ferromagnetic or anti-ferromagnetic; however, all phases converged to a non-magnetic state, and we thus approximate the materials to be non-magnetic. The dynamic stability was investigated through phonon calculations and dispersion plots (see Figure S4). The different MAB phases did not show significant differences as they exhibit positive and real-value modes across the spectrum. Accordingly, it is reasonable to consider all of these phases to be dynamically stable.

The elastic properties of the boride phases were also theoretically investigated. As summarized in Table 1 and Note S2, the calculated elastic constants for MAB phases with M elements from group VI (Cr and Mo) featured slightly stiffer properties than those with M element from group V (V and Nb). However, the latter trend was not seen when going from period IV to V (i.e., MAB phases with Nb is softer than V,

whereas MAB phases with Mo is stiffer than Cr). This observation was based on the elastic constants c_{ij} as well as moduli B_h , G_h , and E_h (see Table 1 and Figure S5). All boride phases showed indications of being brittle, in terms of Pugh and Frantsevich, as well as the two Pettifor criteria (see Figure S5). Even so, the hypothetically ordered $\text{Ta}_4\text{MoSiB}_2$ phase (a solid solution is theoretically predicted and experimentally confirmed in the present paper) exhibited a slightly stiffer property and more brittle characteristic than the other boride phases. Future experimental investigations of the elastic properties are motivated to further confirm the theoretically estimated brittleness.

The electronic density of states (DOS) for the boride phases was theoretically evaluated (see Figure S6). As a general trend, the different boride phases featured metallic characteristics with a sharp valley near the Fermi level. In particular, the Fermi levels ended up above the local minimum for boride phases with Cr or Mo, whereas the Fermi levels for boride phases with V or Nb ended below the local minimum. These findings are in a good agreement with the expected trend as the boride phases with M'' from group VI typically have higher electronic density compared to those phases with M'' from group V. Further insights into the hybridization between Ta, M'' , Si, and B orbitals are discussed in Note S3.

CONCLUSIONS

In summary, we present a solid-state reaction sintering protocol to prepare a computationally driven family of transition metal borides (*o*-MAB phases) with general formula $\text{Ta}_4\text{M}''\text{SiB}_2$ ($\text{M}'' = \text{V}, \text{Cr}$) and a structurally equivalent disordered solid solution $\text{Ta}_4\text{MoSiB}_2$. The $\text{Ta}_4\text{CrSiB}_2$ and

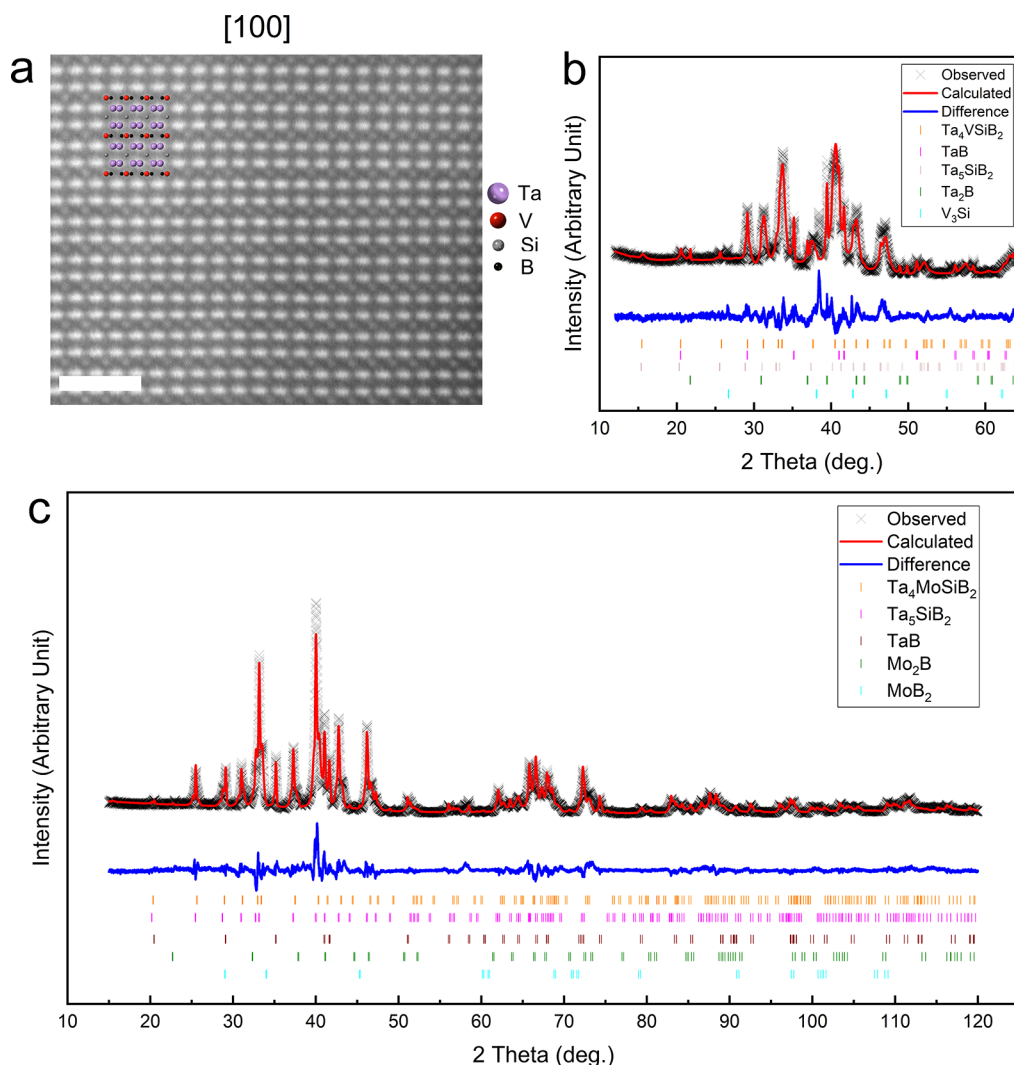


Figure 3. (a) HR-STEM image of the Ta_4VSiB_2 *o*-MAB phase along the zone axes $[100]$ with its corresponding crystal structure overlaid on the image. The scale bar is 1 nm. (b) XRD pattern of the Ta_4VSiB_2 sample showing the measured pattern (black crosses), Rietveld generated pattern (red line), and the difference between both patterns (blue line). The orange, pink, dark red, green, and turquoise ticks (arranged from top to bottom) represent the peak positions of the phases Ta_4VSiB_2 , TaB, Ta_5SiB_2 , Ta_2B , and V_3Si , respectively. (c) XRD pattern of the disordered solid solution $\text{Ta}_4\text{MoSiB}_2$ sample showing the measured pattern (black crosses), Rietveld generated pattern (red line), and the difference between both patterns (blue line). The orange, pink, and dark red, green, and turquoise ticks (arranged from top to bottom) represent the peak positions of the phases $\text{Ta}_4\text{MoSiB}_2$, Ta_5SiB_2 , TaB, Mo_2B , and MoB_2 , respectively.

Ta_4VSiB_2 phases featured a chemically ordered structure as confirmed by atomically resolved HR-STEM imaging. The $\text{Ta}_4\text{MoSiB}_2$ phase formed a thermodynamically stable disordered solid solution alloy in good agreement with theoretical predictions. The XRD analysis combined with Rietveld refinement suggested a high purity of the as-prepared *o*-MAB phases $\text{Ta}_4\text{CrSiB}_2$ (98 wt %) and Ta_4VSiB_2 (81 wt %), while the $\text{Ta}_4\text{MoSiB}_2$ showed a lower purity (41 wt %). The phases were predicted to be dynamically stable, and the calculated electronic density states of MAB phases indicated metallic characteristics though with a sharp local minimum near the Fermi level. Furthermore, the calculated elastic constants of the MAB phases with M'' elements from group VI (Cr and Mo) were stiffer than those with the M'' element from group V (V and Nb).

EXPERIMENTAL AND COMPUTATIONAL METHODS

Synthesis Description. Elemental powders (their characteristic details are given in Table S1) for each desired phase were mixed using an agate mortar and pestle in the atomic ratios corresponding to the targeted stoichiometry, see Table S3. After mixing, the powders were cold pressed into disks of 0.5 cm diameter and 1 cm thickness using a manual hydraulic press with a pressure of 70 kPa. The cold pressed disks were placed in an alumina crucible which was then placed in a horizontal tube furnace. The furnace was heated and cooled at a rate of $5^\circ\text{C}/\text{min}$ under an Ar flow of 5 sccm. The soaking temperature and time are listed in Table S3. After cooling, the samples were crushed into powder using mortar and pestle and sieved through a 450-mesh sieve.

Materials Characterization Techniques. The structure and weight percentage of the phases present in the produced samples were characterized using XRD of the powders by filling a groove of dimensions $20 \times 20 \times 1$ mm in a glass holder. The measurements were conducted using a PANalytical diffractometer equipped with a $\text{Cu K}\alpha$ radiation source (step size = $0.0084^\circ 2\theta$ and time per step = 32

Table 1. Elastic Constants of All Ta₄M''SiB₂ Structures, Including the Hypothetically Ordered Ta–Nb and Ta–Mo Phases for which Solid Solutions (SQS Models) Are Expected^a

	Ta–V	Ta–Cr	(Ta–Nb)	Ta–Nb (SQS)	(Ta–Mo)	Ta–Mo (SQS)
c_{11}	474.1	479.3	474.7	472.7	502.8	492.4
c_{33}	432.5	439.0	432.0	425.5	449.1	445.1
c_{12}	136.3	150.9	124.7	125.7	139.1	134.6
c_{13}	154.0	162.0	146.2	144.6	159.6	156.7
c_{44}	187.4	202.9	174.3	175.1	198.3	189.6
c_{66}	152.1	156.3	148.0	147.1	163.5	150.7
B_h	252.1	260.7	246.1	244.4	263.3	258.4
G_h	166.8	172.2	163.0	162.6	177.4	170.4
E_h	410.0	423.4	400.7	399.2	434.6	419.1
G_h/B_h	0.662	0.661	0.665	0.665	0.674	0.660
ν	0.229	0.229	0.229	0.228	0.225	0.230
$c_{13}-c_{44}$	-33.4	-40.9	-28.1	-30.5	-38.7	-32.9
$c_{12}-c_{66}$	-15.8	-5.4	-23.4	-21.5	-24.5	-16.1

^aThe Hill averages for Bulk, Shear, and Young's Modulus are shown, as well as values for G/B , Poisson ratio ν and Cauchy pressures $c_{13}-c_{44}$ and $c_{12}-c_{66}$, used for assessing ductility.

s). The divergence slits and receiving slit of $1/2^\circ$ and 5 mm, respectively, were used along with a Ni beta filter. To obtain the structural parameters and weight percentages of the phases in a sample, Rietveld refinement of the XRD pattern was performed using FullProf. code.^{19,20} The refined parameters were five background parameters, scale factors (from which the phases' weight percentage was obtained), lattice parameters, X and Y profile parameters, and atomic positions for all the phases, in addition to the global isotropic thermal displacement parameter and asymmetry parameters for the major phases. The dependency of Ta/M''(V, Cr, Mo) intermixing on the refinement was assessed by evaluating χ^2 , and the obtained results were only used if the refinement reduced χ^2 by at least 10%. If not, no intermixing was allowed, and the occupancies were fixed during the refinement.

The microstructure and chemical composition were obtained by SEM, SEM (LEO 1550), combined with an EDX spectrometer. The EDX measurements were acquired from at least 15 particles, all containing Ta, M'', and Si in atomic ratios close to 4:1:1, respectively. Particles that have a stoichiometry close to the secondary phases identified by the XRD Rietveld refinement were excluded. To resolve the atomic structure and ordering of the out-of-plane ordered phases, high-resolution scanning transmission electron microscopy (HR-STEM) imaging was performed using the Linköping double-corrected FEI Titan³ (S)TEM operated at 300 kV, employing a high-angle annular dark-field (HAADF) detector. The HAADF signal intensity of the atomic columns in the STEM images is considered as directly interpretable scaling with atomic number ($\sim Z^{1.7}$).²¹

Computational Methods. First principle calculations were carried out using DFT as implemented in the Vienna ab initio software package (VASP).^{22,23} Exchange–correlation effects were treated within the generalized gradient approximation of Perdew–Burke–Ernzerhof.²⁴ Phonon calculations were carried out using density functional perturbation theory, as implemented in VASP and PhonoPy.²⁵

We started the calculation by relaxing the structures, both with regards to internal atomic structure and cell shape until optimal energy and stress were zero. Using this optimized structure, we carried out further calculations of electronic band structure and DOS as well as determination of elastic constants and phonon dispersions.

The primitive unit cell of a 4112 MAB has a tetragonal symmetry and holds a total of 32 atoms, even as the formula unit Ta₄M''SiB₂ has 8 atoms. The atomic structure is shown in Figure 1. The relaxations were done using a kmesh of $16 \times 16 \times 8$. DOS was calculated with a kmesh of $20 \times 20 \times 10$, while the electronic band structure was determined for a total of 120 points along each symmetry line. In the phonon calculations, we used $2 \times 2 \times 2$ supercells with a $4 \times 4 \times 2$ kmesh. In all calculations, we set the cutoff energies for the plane-wave expansion to 400 eV.

For the disordered structures, we used a 160 atom SQS²⁶ and a kmesh of $5 \times 5 \times 5$ for the relaxations and $7 \times 7 \times 7$ when determining the electronic DOS. The elastic constants were determined by straining the relaxed equilibrium structure along several different directions using strain tensors ϵ . The stress σ was obtained from the VASP output, and the elastic constant tensor C was obtained through the relation $\sigma = C\epsilon$. Details can be found in the supplemental info.

■ ASSOCIATED CONTENT

Supporting Information

The Supporting Information is available free of charge at <https://pubs.acs.org/doi/10.1021/acs.cgd.3c00197>.

EDS, SEM, STEM, Rietveld refinement of the XRD data, theoretical analysis, and methods for elastic constants calculation (PDF)

■ AUTHOR INFORMATION

Corresponding Authors

Ahmed S. Etman – Materials Design Division, Department of Physics, Chemistry and Biology (IFM), Linköping University, Linköping SE-58183, Sweden; orcid.org/0000-0003-0358-2379; Email: ahmed.etman@kemi.uu.se

Johanna Rosen – Materials Design Division, Department of Physics, Chemistry and Biology (IFM), Linköping University, Linköping SE-58183, Sweden; orcid.org/0000-0002-5173-6726; Email: johanna.rosen@liu.se

Authors

Joseph Halim – Materials Design Division, Department of Physics, Chemistry and Biology (IFM), Linköping University, Linköping SE-58183, Sweden; orcid.org/0000-0002-7502-1215

Hans Lind – Materials Design Division, Department of Physics, Chemistry and Biology (IFM), Linköping University, Linköping SE-58183, Sweden

Megan Dorri – Materials Design Division, Department of Physics, Chemistry and Biology (IFM), Linköping University, Linköping SE-58183, Sweden

Justinas Palisaitis – Thin Film Physics Division, Department of Physics, Chemistry and Biology (IFM), Linköping University, Linköping SE-58183, Sweden

Jun Lu – Thin Film Physics Division, Department of Physics, Chemistry and Biology (IFM), Linköping University, Linköping SE-58183, Sweden

Lars Hultman – Thin Film Physics Division, Department of Physics, Chemistry and Biology (IFM), Linköping University, Linköping SE-58183, Sweden

Per O. Å. Persson – Thin Film Physics Division, Department of Physics, Chemistry and Biology (IFM), Linköping University, Linköping SE-58183, Sweden; orcid.org/0000-0001-9140-6724

Complete contact information is available at:
<https://pubs.acs.org/10.1021/acs.cgd.3c00197>

Author Contributions

[§]A.S.E. and J.H.: equal contribution.

Notes

The authors declare no competing financial interest.

ACKNOWLEDGMENTS

J.R. and L.H. acknowledge the support from the Knut and Alice Wallenberg (KAW) Foundation for Fellowship/Scholar Grants and from the Göran Gustafsson foundation. Support from the Swedish Government Strategic Research Area in Materials Science on Functional Materials at Linköping University (Faculty Grant SFO-Mat-LiU No 2009 00971) is also acknowledged. We also thank KAW for support of the electron microscopy laboratory in Linköping and the Swedish Research Council and SSF for access to ARTEMI, the Swedish National Infrastructure in Advanced Electron Microscopy (2021-00171 and RIF21-0026). The calculations were carried out using supercomputer resources provided by the Swedish National Infrastructure for Computing (SNIC), partially founded by the Swedish Research Council through grant agreement no. 2018-05973.

REFERENCES

- (1) Ade, M.; Hillebrecht, H. Ternary Borides Cr₂AlB₂, Cr₃AlB₄, and Cr₄AlB₆: The First Members of the Series (CrB₂)N_xCrAl with n = 1, 2, 3 and a Unifying Concept for Ternary Borides as MAB-Phases. *Inorg. Chem.* **2015**, *54*, 6122–6135.
- (2) Pu, D.; Pan, Y. New Insight into the Structural Stability, Ductility and Melting Point of Mo₅SiB₂ under High-Pressure Environment. *Vacuum* **2022**, *196*, No. 110727.
- (3) Barsoum, M. W. MAX Phases: Properties of Machinable Ternary Carbides and Nitrides. In *MAX Phases*; Wiley Online Books; Wiley-VCH Verlag GmbH & Co. KGaA: Weinheim, Germany, 2013.
- (4) Sokol, M.; Natsu, V.; Kota, S.; Barsoum, M. W. On the Chemical Diversity of the MAX Phases. *Trends Chem.* **2019**, *1*, 210–223.
- (5) Naguib, M.; Kurtoglu, M.; Presser, V.; Lu, J.; Niu, J.; Heon, M.; Hultman, L.; Gogotsi, Y.; Barsoum, M. W. Two-Dimensional Nanocrystals Produced by Exfoliation of Ti₃AlC₂. *Adv. Mater.* **2011**, *23*, 4248–4253.
- (6) VahidMohammadi, A.; Rosen, J.; Gogotsi, Y. The World of Two-Dimensional Carbides and Nitrides (MXenes). *Science* **2021**, *372*, No. eabf1581.
- (7) Ali, M. M.; Hadi, M. A.; Ahmed, I.; Haider, A. F. M. Y.; Islam, A. K. M. A. Physical Properties of a Novel Boron-Based Ternary Compound Ti₂InB₂. *Mater. Today Commun.* **2020**, *25*, No. 101600.
- (8) Rezaie, A. A.; Lee, E.; Yapo, J. A.; Fokwa, B. P. T. Highly Active and Abundant MAB Phases Ni_n+1ZnB_n (n = 1, 2) toward Hydrogen Evolution. *Adv. Energy Sustainability Res.* **2021**, *2*, No. 2100052.
- (9) Rezaie, A. A.; Yan, Z.; Scheifers, J. P.; Zhang, J.; Guo, J.; Fokwa, B. P. T. Synthesis and Li-Ion Electrode Properties of Layered MAB Phases Ni_n+1ZnB_n (n = 1, 2). *J. Mater. Chem. A* **2020**, *8*, 1646–1651.
- (10) Nowotny, H.; Dimakopoulou, E.; Kudielka, H. Untersuchungen in Den Dreistoffsystemen: Molybdän-Silizium-Bor, Wolfram-Silizium-Bor Und in Dem System: VS₂–TaSi₂. *Monatsh. Chem.* **1957**, *88*, 180–192.
- (11) Aronsson, B.; Lundgren, G.; Hansen, S. E.; Sömme, R.; Stenhagen, E.; Palmstierna, H. X-Ray Investigations on Me-Si-B Systems (Me = Mn, Fe, Co). I. Some Features of the Co-Si-B System at 1000 Degrees C. Intermediate Phases in the Co-Si-B and Fe-Si-B Systems. *Acta Chem. Scand.* **1959**, *13*, 433–441.
- (12) Yoshimi, K.; Nakatani, S.; Suda, T.; Hanada, S.; Habazaki, H. Oxidation Behavior of Mo₅SiB₂-Based Alloy at Elevated Temperatures. *Intermetallics* **2002**, *10*, 407–414.
- (13) Ruan, B. B.; Yang, Q. S.; Zhou, M. H.; Chen, G. F.; Ren, Z. A. Superconductivity in a New T₂-Phase Mo₅GeB₂. *J. Alloys Compd.* **2021**, *868*, No. 159230.
- (14) Dahlqvist, M.; Tao, Q.; Zhou, J.; Palisaitis, J.; Persson, P. O. Å.; Rosen, J. Theoretical Prediction and Synthesis of a Family of Atomic Laminate Metal Borides with In-Plane Chemical Ordering. *J. Am. Chem. Soc.* **2020**, *142*, 18583–18591.
- (15) Zhou, J.; Palisaitis, J.; Halim, J.; Dahlqvist, M.; Tao, Q.; Persson, I.; Hultman, L.; Persson, P. O. Å.; Rosen, J. Boridene: Two-Dimensional Mo_{4/3}B_{2-x} with Ordered Metal Vacancies Obtained by Chemical Exfoliation. *Science* **2021**, *373*, 801–805.
- (16) Helmer, P.; Halim, J.; Zhou, J.; Mohan, R.; Wickman, B.; Björk, J.; Rosen, J. Investigation of 2D Boridene from First Principles and Experiments. *Adv. Funct. Mater.* **2022**, *32*, No. 2109060.
- (17) Dahlqvist, M.; Zhou, J.; Persson, I.; Ahmed, B.; Lu, J.; Halim, J.; Tao, Q.; Palisaitis, J.; Thörnberg, J.; Helmer, P.; Hultman, L.; Persson, P. O. Å.; Rosen, J. Out-Of-Plane Ordered Laminate Borides and Their 2D Ti-Based Derivative from Chemical Exfoliation. *Adv. Mater.* **2021**, *33*, No. 2008361.
- (18) Dahlqvist, M.; Rosen, J. Chemical Order or Disorder – a Theoretical Stability Expose for Expanding the Compositional Space of Quaternary Metal Borides. *Mater. Adv.* **2022**, *3*, 2908–2917.
- (19) Rietveld, H. M. A Profile Refinement Method for Nuclear and Magnetic Structures. *J. Appl. Crystallogr.* **1969**, *2*, 65–71.
- (20) Rodríguez-Carvajal, J. Recent Advances in Magnetic Structure Determination by Neutron Powder Diffraction. *Phys. B: Condens. Matter* **1993**, *192*, 55–69.
- (21) Pennycook, S. J.; Boatner, L. A. Chemically Sensitive Structure-Imaging with a Scanning Transmission Electron Microscope. *Nature* **1988**, *336*, 565–567.
- (22) Kresse, G.; Hafner, J. Ab Initio Molecular-Dynamics Simulation of the Liquid-Metal–Amorphous-Semiconductor Transition in Germanium. *Phys. Rev. B: Condens. Matter Mater. Phys.* **1994**, *49*, 14251–14269.
- (23) Kresse, G.; Furthmüller, J. Efficient Iterative Schemes for Ab Initio Total-Energy Calculations Using a Plane-Wave Basis Set. *Phys. Rev. B: Condens. Matter Mater. Phys.* **1996**, *54*, 11169–11186.
- (24) Perdew, J. P.; Burke, K.; Ernzerhof, M. Generalized Gradient Approximation Made Simple. *Phys. Rev. Lett.* **1996**, *77*, 3865–3868.
- (25) Togo, A.; Tanaka, I. First Principles Phonon Calculations in Materials Science. *Scr. Mater.* **2015**, *108*, 1–5.
- (26) Zunger, A.; Wei, S.-H.; Ferreira, L. G.; Bernard, J. E. Special Quasirandom Structures. *Phys. Rev. Lett.* **1990**, *65*, 353–356.